ChemPubSoc Europe

DOI: 10.1002/chem.201503432

CHEMISTRY A European Journal Full Paper

Heterogeneous Catalysis

Clean Synthesis of an Economical 3D Nanochain Network of PdCu Alloy with Enhanced Electrocatalytic Performance towards Ethanol Oxidation

Jiawei Liu, Zhao Huang, Kai Cai, Huan Zhang, Zhicheng Lu, Tingting Li, Yunpeng Zuo, and Heyou Han*[a]

Abstract: A one-pot method for the fast synthesis of a 3D nanochain network (NNC) of PdCu alloy without any surfactants is described. The composition of the as-prepared PdCu alloy catalysts can be precisely controlled by changing the precursor ratio of Pd to Cu. First, the Cu content changes the electronic structure of Pd in the 3D NNC of PdCu alloy. Second, the 3D network structure offers large open pores, high surface areas, and self-supported properties. Third, the surfactant-free strategy results in a relatively clean surface. These factors all contribute to better electrocatalytic activity and durability towards ethanol oxidation. Moreover, the use of copper in the alloy lowers the price of the catalyst by replacing the noble metal palladium with non-noble metal copper. The composition-optimized $Pd_{80}Cu_{20}$ alloy in the 3D NNC catalyst shows an increased electrochemically active surface area (80.95 $m^2 g^{-1}$) and a 3.62-fold enhancement of mass activity (6.16 $A mg^{-1}$) over a commercial Pd/C catalyst.

Introduction

The last several decades have witnessed great advances in noble-metal-based electrocatalysts for direct ethanol fuel cells (DEFCs) because state-of-the-art commercial Pt/C anode catalysts need to be replaced due to their high cost, relatively low catalytic activity, and poor durability.[1,2] A promising solution to solve all of these problems is to synthesize shape-controlled alloy catalysts.[3] First, it is possible to reduce the loading of platinum by alloying or replacing platinum with other transition metals; this mainly contributes to lowering the cost.[4,5] Second, the alloy nature has a positive effect on the catalytic activity and durability.[6,7] Additionally, shape-controlled catalysts always show perfect catalytic activity because of their large surface areas.[8]

Palladium is a suitable replacement for platinum not only due to its larger earth abundance, but also because of its good performance as an electrocatalyst towards ethanol.[9,10] Previous studies have reported many Pd-based shape-controlled catalysts, such as PdNi nanoparticles (NPs),[11] PdAu nanochains,[12] and PdPt nanotubes,[13,14] with good catalytic activity. Apart from these, 3D nanochain networks (NNCs) are promising shape-controlled catalysts, which have the advantages of large surface area, as well as superior physical and chemical properties due to the combination of the specific properties of nanomaterials magnified by self-assembly on the macroscale.[15] Various NNCs have been used in electrocatalytic ethanol oxidation, such as Pd NNCs,[16] PdAu NNCs,[17,18] and PdPt NNCs,[6] all of which perform better than the commercial Pd/C catalyst.

However, most of these methods require either the preproduction of metal NPs in the first step or the addition of template, surfactant, and stabilizer; thus making the preparation process complicated and time consuming, which limits their large-scale production. Furthermore, added surfactants have negative effects on the properties of these materials and surfactant-removing processes are always difficult or required to be performed under harsh conditions.[19–22] In addition, many studies used another noble metal as the alloy content, which contributes little to decreasing the amount of noble metal. Therefore, it is crucial to develop a clean and fast synthetic approach without involving surfactants or another noble metal in preparing economical 3D alloy NNC catalysts with enhanced performance towards ethanol electro-oxidation.

Herein, we reported a one-pot salt-mediated self-assembly method for the rapid synthesis of PdCu 3D NNCs in the absence of surfactants. Not only does alloying with copper improve the electrocatalytic activity, but also it lowers the price of the catalyst. Research into the mechanism of forming network structures revealed that cations enable the NPs to aggregate, and higher valence cations have a stronger ability to fabricate the network structures because the minimum concentrations of cations required to form 3D NNCs decrease with increasing valence. On the other hand, anions facilitate the ani-

[a] J. Liu, Z. Huang, K. Cai, H. Zhang, Dr. Z. Lu, T. Li, Y. Zuo, Prof. H. Han
State Key Laboratory of Agriculture Microbiology
College of Science, College of Food Science and Technology
Huazhong Agricultural University
Wuhan 430070 (P.R. China)
E-mail: hyhan@mail.hzau.edu.cn

Supporting information for this article is available on the WWW under http://dx.doi.org/10.1002/chem.201503432.

sotropic growth of NPs. The versatility of this method was also tested by fabricating PdPt and PdAu alloys of 3D NNCs.

The morphology of the PdCu 3D network structure was observed by SEM and (high-resolution (HR)) TEM, and the alloy nature of this 3D NNC was confirmed by XRD. The electrocatalytic performance for ethanol oxidation with the PdCu 3D network was evaluated in alkaline solution. The composition-optimized $Pd_{80}Cu_{20}$ 3D NNC had an enhanced electrocatalytic mass activity (6.16 A mg^{-1}) as well as better durability than that of a commercial Pd/C catalyst. Our results demonstrate that the performance of the electrocatalyst prepared by a surfactant-free strategy can be significantly enhanced.

Results and Discussion

The porous structures of the as-prepared $Pd_{80}Cu_{20}$ 3D NNCs were confirmed by SEM (Figure 1 A) and TEM (Figure 1 B and C). The TEM images demonstrate that the porous networks consist of ultrathin primary nanochains with a relatively uniform diameter of 6.8 nm. As shown in Figure 1 D, the electron diffraction pattern of $Pd_{80}Cu_{20}$ 3D NNC consists of diffraction rings rather than separated spots, which indicates that the PdCu 3D NNC is polycrystalline, as further observed in HRTEM images and XRD patterns.

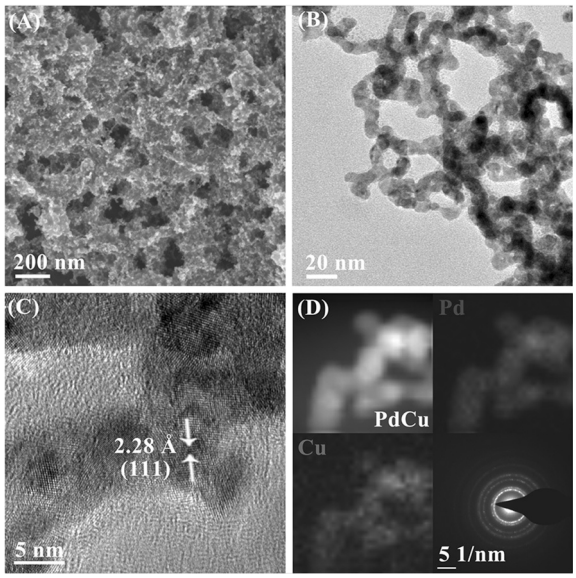

Figure 1. TEM (A and B) and HRTEM (C) images and D) high-angle annular dark-field scanning electron microscopy (HAADF-STEM) elemental mapping and electron diffraction pattern of the PdCu 3D NNC.

The composition of the $Pd_{80}Cu_{20}$ 3D NNC was analyzed by inductively coupled plasma atomic emission spectroscopy (ICP-AES). The mass ratio of Pd to Cu in $Pd_{80}Cu_{20}$ NNC is about 4:1, whereas the atomic ratio is about 7:3, which is different from the precursor ratio because $PdCl_4^-$ has a higher reaction rate than Cu^{2+}. When the precursor ratio of Pd to Cu was regulated, $Pd_{68}Cu_{32}$ and $Pd_{59}Cu_{41}$ 3D NNCs with different mass ratios of Pd to Cu were also fabricated. When evaluating the electrocatalytic activity of multimetallic structures, the state of alloying is an important index. Recently, Eychmüller et al. showed separated phases in their original multimetallic 3D NNCs, and only after several hours of heat treatment at 400 °C under an inert atmosphere could the separated phases be transformed into an alloy; this raises the question of whether or not our PdCu 3D NNCs are alloys.[23] From HAADF-STEM elemental mapping of $Pd_{80}Cu_{20}$ 3D NNC (Figure 1 D), we can see the uniform dispersity of Pd and Cu in this network structure, which means that it is an alloy rather than core–shell structures or separated phases. To gain more insights into this issue, the PdCu 3D NNCs were analyzed by powder XRD.

Figure 2 shows the XRD patterns of $Pd_{80}Cu_{20}$, $Pd_{68}Cu_{32}$, $Pd_{59}Cu_{41}$, and Pd 3D NNCs with all of the peaks corresponding

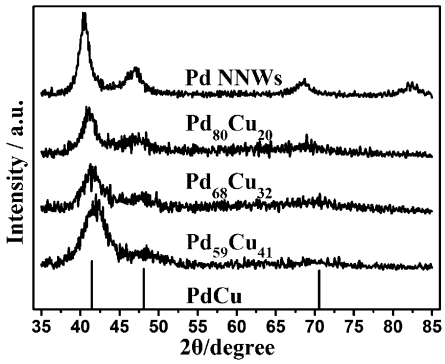

Figure 2. XRD patterns of $Pd_{80}Cu_{20}$, $Pd_{68}Cu_{32}$, $Pd_{59}Cu_{41}$, and Pd 3D NNCs.

to the cubic phase. The peaks of PdCu 3D NNCs are all around those of PdCu (JCPDS 048-1551), and they shift positively with increasing mass fraction of Cu, which reveals that the lattice constants of the PdCu alloys are larger than those of pure Pd NNC as a result of the alloying of Cu with a smaller atomic radius.[18] In addition, there are no separated Pd and Cu reflection peaks, which indicates that the PdCu 3D NNCs are alloys instead of heterostructures or separate nanonets.[24] A similar phenomenon can also be observed in PdAu and PdPt 3D NNCs (Figures S1 and S2 in the Supporting Information). These results indicated that our method was successful for the fabrication of different kinds of bimetallic 3D NNCs; this method is much easier to use than those previously reported. More importantly, this method offers the possibility of synthesizing tri- or multimetallic alloys in a facile manner.

Changes to the surface electronic structure of Pd in the PdCu 3D NNCs was investigated by X-ray photoelectron spectroscopy (XPS; Figure 3). The binding energies of Pd $3d_{5/2}$ for $Pd_{80}Cu_{20}$, $Pd_{68}Cu_{32}$, and $Pd_{59}Cu_{41}$ 3D NNCs are 335.051, 334.751, and 334.501 eV, respectively, which are evidently lower than that of pure Pd NNC (335.601 eV) and negatively shifted to lower binding energy with decreasing Pd/Cu ratios.[25,26] The binding energy shift of Pd indicates a visible change in the electronic structure, due to intra-atomic charge transfer or interatomic charge transfer between Pd and Cu when they are alloyed together in the PdCu 3D NNC; this might influence the

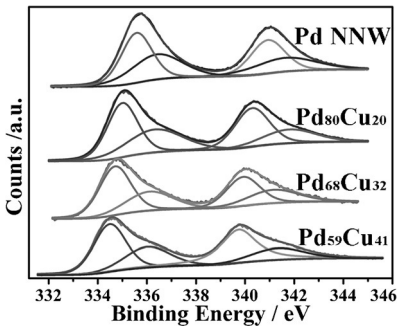

Figure 3. XPS results for $Pd_{80}Cu_{20}$ and Pd 3D NNCs.

activity and durability of the electrocatalytic ethanol oxidation reaction.[18]

To explore the mechanism for the formation of these 3D NNCs, we first use Pd 3D NNC as a model to understand the function of salt in these reactions. These palladium nanochains are fused and interconnected at various angles, and some of them are connected along the nanochain direction to form a branch-type structure. Different lattices of some typical spots, including cross-linked points, curved turning parts, and nanochains with free branch ends, are shown in Figure 4. Lattice planes with an interplanar distance of about 2.30 Å, considered to be the (111) plane of face-centered cubic (fcc) metallic Pd, are widely distributed at all locations, and the 1/3(422), (200), and (220) planes are also found in different places.

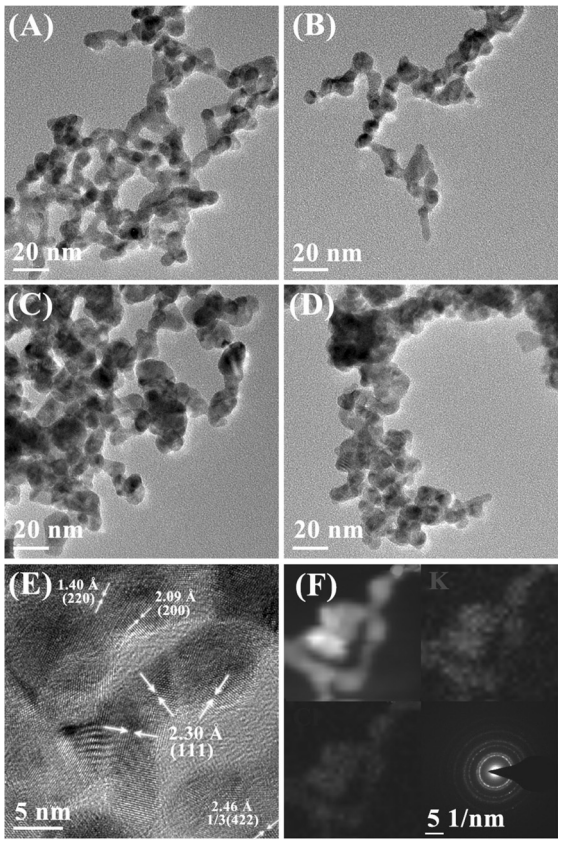

Figure 4. TEM micrographs of Pd 3D NNCs synthesized with different concentrations of cations: A) 37.8 mM KCl, B) 0.75 mM $CaCl_2$, C) 12.5 μM $AlCl_3$, and D) 12.5 mM $AlCl_3$. E) HRTEM micrograph. F) Electron diffraction pattern and STEM energy-dispersive X-ray spectroscopy (EDX) mapping of K and Cl for the sample shown in A).

In this process, we used different amounts and valences of cations, including K^+, Na^+, Ca^{2+}, Mg^{2+}, Zn^{2+}, Al^{3+}, and Cr^{3+}, to control the reaction and found that the minimum concentration of cations to form Pd 3D NNCs decreased with increasing valence and approximately obeyed the following regulation: $X^+/Y^{2+}/Z^{3+} = 3000:60:1$, in which X^+ indicates a monovalent cation, Y^{2+} indicates a divalent cation, and Z^{3+} indicates a trivalent cation; this means that higher valence cations have stronger abilities to fabricate network structures. Detailed data are given in Table S1 in the Supporting Information and the characterizations of the morphologies are shown in Figure 4 and Figure S3 in the Supporting Information. If anions played an important role in this stage, the difference between the minimum concentrations would be minor. Furthermore, upon increasing the amount of cations, the staking effect of palladium nanostructures becomes more influential (Figure 4D).

In previous studies, Zheng et al. demonstrated that some trivalent cations, such as Fe^{3+} and Al^{3+}, were able to assemble 2D surfactant-free Pd nanosheets into 1D Pd superlattice nanowires in a face-to-face manner.[27] From some (111) planes of fcc metallic Pd in the cross-linked point shown in the HRTEM image in Figure 4E, it can be deduced that cations play a significant role in the present study. Specifically, the original metal particles were coated by borate (the production of reductant), whereas cations worked as the ion binder to connect different metal particles through electrostatic adsorption, and an overall distribution of potassium along the nanobranches was found in the metal network, as confirmed by STEM-EDX analysis (Figure 4F). In addition, because higher valence cations have stronger affinities for borate, they should also have a stronger ability to form these network structures, which is in accordance with the aforementioned rule.

To further test this hypothesis, we synthesized the palladium NP first, followed by the addition of KCl to fabricate the 3D NNC structures (Figure S4A in the Supporting Information). However, there were many differences between these 3D NNCs. The grain structures in the nanochains of each network increased with increasing valence of each cation, and the number of these grain structures reached the peak shown in Figure S4 in the Supporting Information. After analyzing these reaction conditions, we found that the concentrations of anions contributed most to the formation of these grain nanostructures. Previous studies showed that monovalent Cl^- favored the anisotropic growth of NPs by specifically binding onto the (100) facets of fcc nanocrystals, thus restricting the growth of (100) facets, and an overall distribution of Cl along the nanobranches was also found in the metal network, which could be confirmed by STEM-EDX (Figure 4F).[28,29] Therefore, we assumed that the nanostructures of the branches could be controlled by tuning the concentration and type of anions.

To confirm this assumption, we performed some control experiments by replacing Cl^- with Br^-, NO_3^-, and SO_4^{2-} anions. As shown in Figure S4 in the Supporting Information, the grain

structures increased in the order of Br^-, NO_3^-, and SO_4^{2-}; this means that Cl^- and Br^- have the strongest ability to form these grain structures. The multigrain structures shown in Figure S4A in the Supporting Information can be attributed to the lack of anions to restrict growth of the (100) facets of the NPs in the first stage, and thus, the addition of KCl only leads to the assembly of NPs into networks with a large number of grain structures. This result further confirmed the occurrence of the restricting effect of anions in the growth of palladium NPs.

However, it is impossible to synthesize Cu NNCs by this method, which makes it harder to fabricate PdCu 3D NNCs. Only by adding both KCl and $AlCl_3$ can the PdCu 3D NNC be formed (Figure S5 in the Supporting Information).

Moreover, the amount of precursors also affects the NNC: 0.125 mM of precursors leads to a very low production, whereas 0.5 mM of precursors results in the aggregation of nanomaterials; thus breaking the network structures, and therefore, 0.25 mM of precursors is appropriate (Figure S6 in the Supporting Information).

In addition, sodium borohydride plays an important role in this reaction because of its strong reducing capacity. After adding sodium borohydride, many NPs formed immediately, which provided the original materials for the NNC. When using other reducing agents, such as ascorbic acid and hydrazine hydrate, to replace sodium borohydride, we failed to fabricate the PdCu 3D NNC. As result of their weak reducing capacities, only a small amount of NPs emerged in the first stage. There is a main kinetic barrier to forming nuclei in a homogeneous solution because extremely small nuclei are less stable than subsequently formed larger NPs.[30] Therefore, the use of ascorbic acid and hydrazine hydrate as reducing agents would lead to the formation of larger nanostructures instead of NNCs (Figure S7 in the Supporting Information).

The mechanism for the formation of 3D NNCs can be described as follows: sodium borohydride reduces the metal precursor into small NPs coated with borate, and anions facilitate the anisotropic growth of NPs, while cations contribute to the assembly of these small NPs into network structures through electrostatic adsorption (Scheme 1).

Inspired by the attractive nanostructure and properties (3D porous, large surface area, surfactant-free) of PdCu 3D NNC, we tested the electrocatalytic activity of this catalyst towards ethanol oxidation. The electrochemically active surface areas (ECSAs) of PdCu, Pd 3D NNCs, and commercial Pd/C catalysts were estimated by calculating CO stripping results from cyclic voltammograms (CVs) recorded in 0.1 M $HClO_4$ (Figure 5). By assuming that the oxidation of a monolayer of CO on Pd corresponds to a charge of 420 $\mu C\,cm^{-2}$ and normalizing the value by Pd loading, the ECSAs of $Pd_{80}Cu_{20}$, $Pd_{68}Cu_{32}$, and $Pd_{59}Cu_{41}$ 3D NNCs were calculated to be 80.95, 75.36, and 75.1 $m^2\,g^{-1}$, respectively, which were much larger than those of Pd NNCs (63.02 $m^2\,g^{-1}$) and commercial Pd/C (57.91 $m^2\,g^{-1}$). By alloying Cu into PdCu 3D NNCs, the ECSA value was significantly enhanced.[31] However, as the Cu mass amount increased to 32%, there was a slight decrease in ECSA, which might be because the absorbed strength of CO on the PdCu surface was too weak.

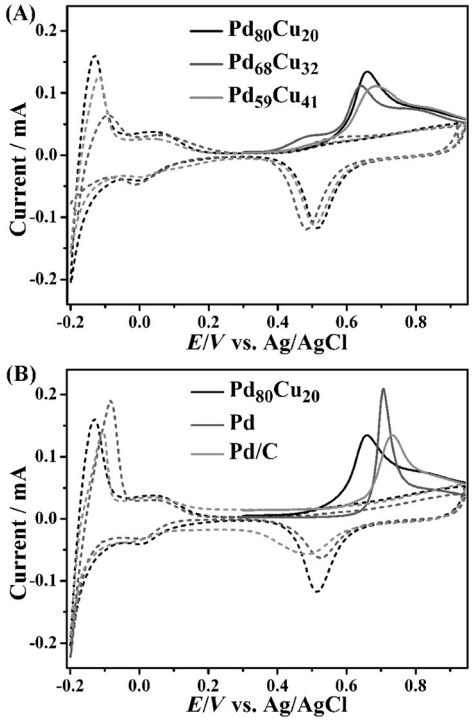

Figure 5. CV (dashed lines) and CO stripping curves (solid lines) of PdCu 3D NNC, Pd 3D NNC, and commercial Pd/C catalysts recorded in 0.1 M $HClO_4$ with a potential sweeping rate of 50 $mV\,s^{-1}$. The Pd mass amounts in the $Pd_{80}Cu_{20}$, $Pd_{68}Cu_{32}$, $Pd_{59}Cu_{41}$, Pd 3D NNCs, and Pd/C catalysts were 1.04, 1.09, 1.05, 1.014, and 1 μg, respectively, as measured by ICP-AES.

It should be noted that there was a clear negative onset potential shift of CO oxidation for PdCu 3D NNCs compared with those of Pd NNC and commercial Pd/C. This also implies that the strength of CO on the PdCu 3D NNCs was weaker, and the removal of CO species only required a lower overpotential; this indicates that the PdCu 3D NNCs have a better tolerance toward CO poisoning than Pd NNC or commercial Pd/C.

Figure 6 shows the CVs of the PdCu, Pd 3D NNCs and state-of-the-art commercial Pd/C catalyst modified electrodes for ethanol oxidation at a scan rate of 50 $mV\,s^{-1}$ in a solution of

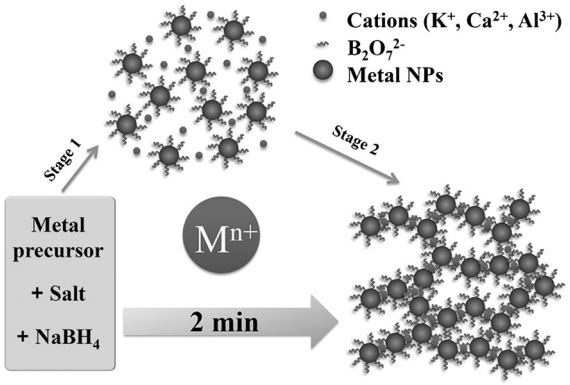

Scheme 1. Formation of metal NNCs from various metal precursors.

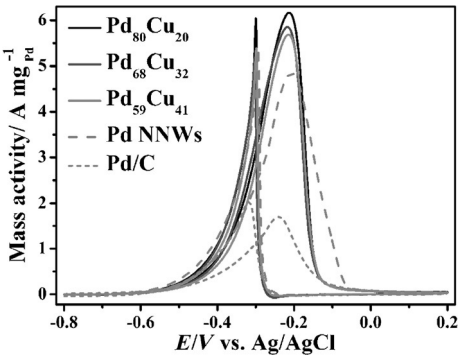

Figure 6. CVs of the PdCu alloy NNCs, Pd NNC, and commercial Pd/C catalyst modified electrodes in 1 M KOH + 1 M ethanol at a scan rate of 50 mV s^{-1} versus Ag/AgCl (3 M KCl). The Pd mass amounts of all the catalysts were in accordance with those in the CO stripping experiments.

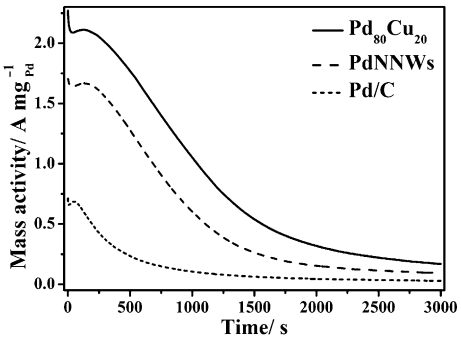

Figure 7. Chronoamperometric curves of the $Pd_{80}Cu_{20}$ alloy NNC, Pd NNC, and commercial Pd/C catalyst modified electrodes in 1 M KOH + 1 M ethanol at −0.3 V versus Ag/AgCl (3 M KCl). The Pd mass amounts of all catalysts were in accordance with those in the CO stripping experiments.

1 M KOH + 1 M ethanol. $Pd_{80}Cu_{20}$ 3D NNC shows the highest activity toward ethanol oxidation in terms of peak current (6.16 A mg^{-1}; 3.62-fold that of commercial Pd/C (1.7 A mg^{-1})), whereas Pd NNC has a much lower activity (4.84 A mg^{-1}), which might mainly be attributed to the largest ECSA and alloy nature of PdCu 3D NNC. Moreover, the forward peak potentials (E_f) of ethanol oxidation on PdCu 3D NNCs are more negative than that of Pd 3D NNC. The negative shift of E_f can be attributed to the modification of the Pd d-band electronic structure by Cu alloying. The lower peak potential contributes to a lower activation barrier toward ethanol oxidation.

Based on the ECSA values determined by CO stripping results, the $Pd_{80}Cu_{20}$ 3D NNC and Pd 3D NNC had much larger area specific currents than that of commercial Pd/C. This indicated that $Pd_{80}Cu_{20}$ 3D NNC (7.61 mA cm^{-2}) and Pd 3D NNC (7.68 mA cm^{-2}) also had better intrinsic electrocatalytic abilities than that of the commercial Pd/C (2.94 mA cm^{-2}); this might be mainly attributed to the network structure in the NNCs. These results reveal that alloying copper into palladium is able to enhance the electrocatalytic activity and efficiency towards ethanol oxidation.

Generally, the forward scan peak current is regarded as representing the oxidation of freshly chemisorbed alcohol species, whereas the reverse scan peak is related to the removal of carbonaceous species that are not completely oxidized in the forward scan.[32] The ratio of the forward anodic peak current (I_f) to the reverse anodic peak current (I_b) usually reflects the tolerance to carbonaceous species accumulation of different catalysts. However, Sun et al. proved that I_f and I_b shared the same chemical origin and both of them represented the oxidation of freshly chemisorbed alcohol species.[33] Therefore, the current ratio criterion is an inadequate parameter to evaluate the CO tolerance of electrocatalysts for the ethanol oxidation reaction.

To further test the stability of the PdCu 3D NNC catalyst, we used a long-term current–time measurement technique, which was carried out at −0.3 V (vs. Ag/AgCl) for 3000 s in a solution containing 1 M potassium hydroxide and 1 M ethanol. From the results shown in Figure 7, it can be seen that the current decay and final current for ethanol oxidation of PdCu 3D NNC is much slower and higher than those of commercial Pd/C catalysts, which means that PdCu 3D NNC has better durability during the reaction. In addition, the morphology of PdCu 3D NNC remained unchanged after this stability test (Figure S8 in the Supporting Information), which further confirmed the good durability of PdCu 3D NNC. Both activity and durability experiments indicate that the PdCu 3D NNC is a promising electrocatalyst for ethanol oxidation; detailed data obtained from the electrocatalytic experiment are shown in Table S2 in the Supporting Information.

The high activity and durability of PdCu 3D NNC can be attributed to the following reasons: 1) The surfactant-free synthesis strategy offers a relatively clean surface for the as-prepared PdCu 3D NNC without an additional surfactant-removing process that requires harsh conditions, which always causes deformation of the nanocrystals and a decrease in catalytic activities. 2) The network structure enhances the intrinsic electrocatalytic ability, which can be observed in the area-specific activities of both PdCu 3D NNC and Pd 3D NNC. 3) It is known that the typical intermediates (CH_3CO_{ad} and CO_{ad}) are strongly adsorbed on Pd surfaces, whereas the incorporation of Cu can weaken the absorbed strength of oxygenated intermediates on the Pd surface, which facilitates the oxidative removal of these intermediates and promotes the overall reaction rate. Therefore, both the catalytic activity and durability are increased because of alloying Cu into these 3D NNCs. However, as the mass fraction of Cu was further increased to more than 20%, the absorbed strength of intermediates on the PdCu surface was too weak to activate the absorbed intermediate, which led to the reduced activity for the $Pd_{68}Cu_{32}$ and $Pd_{59}Cu_{41}$ 3D NNCs relative to that of the $Pd_{80}Cu_{20}$ 3D NNC. 4) The unsupported PdCu 3D NNCs could efficiently avoid the current drop caused by corrosion of the carbon support.

Conclusion

This is probably the first report on the development of a one-pot salt-mediated method for the rapid synthesis of surfactant-free PdCu 3D NNC electrocatalysts. The reaction only lasted 3 min and was performed at room temperature; thus promoting efficiency and cost savings. Analyses of the mechanism of forming these PdCu 3D NNC structures revealed that cations

mainly contributed to the aggregation of NPs to form network frames, whereas anions mainly facilitated the anisotropic growth of NPs. Moreover, other 3D NNCs, such as PdAu and PdPt, can also be prepared by a similar method, which suggests the prevalence of this synthetic strategy. Because of their clean surface, network structure, alloy nature, and lack of support, these PdCu 3D NNCs showed enhanced electrocatalytic activity and durability towards ethanol oxidation over the commercial Pd/C catalyst in alkaline medium. Therefore, this method can be easily applied to synthesize various 3D NNCs with superior properties as catalysts in large-scale production.

Experimental Section

Chemicals

$PdCl_2$ (AR), $H_2PtCl_6{\cdot}6H_2O$ (AR), $HAuCl_4{\cdot}4H_2O$ (AR), $CuCl_2{\cdot}2H_2O$, $AlCl_3{\cdot}6H_2O$ (AR), $CrCl_3{\cdot}6H_2O$ (AR), $CaCl_2$ (AR), $MgCl_2{\cdot}6H_2O$ (AR), $ZnCl_2$ (AR), KCl (AR), KBr (AR), KNO_3 (AR), K_2SO_4 (AR), and $NaBH_4$ (96%) were supplied by Sinopharm Chemical Reagent Co., Ltd (Shanghai, P.R. China). Ultrapure water with a conductivity of 18.25 MΩ cm was used throughout the experiments, and all chemicals were used without further purification.

Preparation of PdCu 3D NNCs

In a typical synthesis, $PdCl_2$ (15, 7.5, or 5 μmol), $CuCl_2$ (15, 22.5, or 25 μmol), KCl (3 mmol), $AlCl_3$ (12 μmol), and water (237 mL) were mixed together and stirred to form a homogeneous solution, followed by the rapid injection of freshly prepared, ice-cold reducing agent solution (3 mL) containing $NaBH_4$ (3 mg). After injection, the solution turned yellow–gray immediately and the $Pd_{80}Cu_{20}$, $Pd_{68}Cu_{32}$, or $Pd_{59}Cu_{41}$ 3D NNC was formed in 3 min. Finally, the products were collected by centrifugation and washed with water.

Preparation of PdAu and PdPt 3D NNCs

In a typical synthesis, $PdCl_2$ (15 μmol), $HAuCl_4$ (or H_2PtCl_6; 15 μmol), KCl (3 mmol), and water (237 mL) were mixed together and stirred to form a homogeneous solution, followed by the rapid injection of freshly prepared, ice-cold reducing agent solution (3 mL) containing $NaBH_4$ (3 mg). After injection, the solution turned dark purple immediately (dark gray for PdPt) and the PdAu (PdPt) 3D NNCs were formed in 3 min. Finally, the products were collected by centrifugation and washed with water.

Preparation of Pd 3D NNCs by different cation and anion

In a typical synthesis, $PdCl_2$ (30 μmol), KCl (3 mmol; or 180 μmol of $CaCl_2$, $MgCl_2$, or $ZnCl_2$; 3 μmol of $AlCl_3$ or $CrCl_3$; 3 mmol of NaCl, KBr, KNO_3, or K_2SO_4) and water (237 mL) were mixed together and stirred to form a homogeneous solution. Then, freshly prepared, ice-cold reducing agent solution (3 mL) containing $NaBH_4$ (3 mg) was injected into the solution rapidly. After injection, the solution became dark gray immediately and the Pd 3D NNCs were formed in 3 min. Finally, the products were collected by centrifugation and washed with water.

Characterization

A field-emission scanning electron microscope (Zeiss Ultra Plus, Germany) was used to record the SEM images. TEM measurements were recorded by using a JEM-2100F high-resolution transmission electron microscope at an accelerating voltage of 200 kV. STEM elemental maps were made in HAADF mode on a FEI TECNAIF-30 microscope operated at 300 kV. Samples for TEM analysis were prepared by depositing a single drop of diluted nanostructure dispersion in water on copper grids. A Bruker D8 Advance X-ray diffractometer equipped with a $Cu_{K\alpha}$ radiation source was used to carry out the XRD analysis of all samples. X-ray photoelectron spectra were measured by using a Thermo VG Multilab 2000 spectrometer equipped with a monochromatic $Al_{K\alpha}$ radiation source at room temperature. ICP-AES measurements were performed on an IRIS Intrepid II XSP instrument (Thermo Fisher Scientific, USA).

Electrochemical characterization

The ethanol oxidation reaction electrochemical measurements were conducted in a three-electrode cell that consisted of a glassy carbon electrode (GC; 3 mm in diameter), a platinum wire counter electrode, and an Ag/AgCl (saturated KCl) reference electrode by using a CHI 660D electrochemical workstation from CH Instruments, Inc. Before the electrochemical test, the GC electrode was polished carefully with 1.0, 0.3, and 0.05 μm alumina powder successively, rinsed with deionized water, followed by sonication in 8 M HNO_3 and deionized water, respectively. Then, the electrode was allowed to dry under nitrogen. For all electrochemical tests, aqueous solutions (6 μL) of PdCu NNCs and commercial Pd/C catalyst were dropped on each electrode and dried at room temperature. Then, 0.28% Nafion (5 μL; diluted from 5% Nafion, Aldrich) was added and dried before the test. The Pd mass amounts of $Pd_{80}Cu_{20}$, $Pd_{68}Cu_{32}$, $Pd_{59}Cu_{41}$, Pd NNCs, and Pd/C catalysts on the surface of the GC electrode were 1.04, 1.09, 1.05, 1.014, and 1 μg, respectively, as measured by ICP-AES.

Acknowledgements

We acknowledge financial support from the National Natural Science Foundation of China (21375043, 21175051).

Keywords: alloys · copper · electrochemistry · nanostructures · palladium

[1] E. Antolini, *J. Power Sources* **2007**, *170*, 1–12.
[2] F. Vigier, C. Coutanceau, A. Perrard, E. M. Belgsir, C. Lamy, *J. Appl. Electrochem.* **2004**, *34*, 439–446.
[3] J. J. Lv, L. P. Mei, X. Weng, A. J. Wang, L. L. Chen, X. F. Liu, J. J. Feng, *Nanoscale* **2015**, *7*, 5699–5705.
[4] R. Jiang, D. T. Tran, J. P. McClure, D. Chu, *ACS Catal.* **2014**, *4*, 2577–2586.
[5] K. Cai, J. Liu, H. Zhang, Z. Huang, Z. Lu, M. F. Foda, T. Li, H. Han, *Chem. Eur. J.* **2015**, *21*, 7556–7561.
[6] C. Zhu, S. Guo, S. Dong, *Chem. Eur. J.* **2013**, *19*, 1104–1111.
[7] B. Y. Xia, H. B. Wu, X. Wang, X. W. Lou, *J. Am. Chem. Soc.* **2012**, *134*, 13934–13937.
[8] Y. Zuo, K. Cai, L. Wu, T. Li, Z. Lv, J. Liu, K. Shao, H. Han, *J. Mater. Chem. A* **2015**, *3*, 1388–1391.
[9] F. a. Ksar, L. Ramos, B. Keita, L. Nadjo, P. Beaunier, H. Remita, *Chem. Mater.* **2009**, *21*, 3677–3683.
[10] C. Bianchini, P. K. Shen, *Chem. Rev.* **2009**, *109*, 4183–4206.
[11] S. Y. Shen, T. S. Zhao, J. B. Xu, Y. S. Li, *J. Power Sources* **2010**, *195*, 1001–1006.
[12] C. Zhu, S. Guo, S. Dong, *Adv. Mater.* **2012**, *24*, 2326–2331.
[13] S. Guo, S. Dong, E. Wang, *Energy Environ. Sci.* **2010**, *3*, 1307.
[14] Z. Huang, H. Zhou, F. Sun, C. Fu, F. Zeng, T. Li, Y. Kuang, *Chem. Eur. J.* **2013**, *19*, 13720–13725.

[15] W. Liu, A. K. Herrmann, N. C. Bigall, P. Rodriguez, D. Wen, M. Oezaslan, T. J. Schmidt, N. Gaponik, A. Eychmuller, *Acc. Chem. Res.* **2015**, *48*, 154 – 162.
[16] W. Liu, A. K. Herrmann, D. Geiger, L. Borchardt, F. Simon, S. Kaskel, N. Gaponik, A. Eychmuller, *Angew. Chem. Int. Ed.* **2012**, *51*, 5743 – 5747; *Angew. Chem.* **2012**, *124*, 5841 – 5846.
[17] W. Hong, J. Wang, E. Wang, *ACS Appl. Mater. Interfaces* **2014**, *6*, 9481 – 9487.
[18] L. Y. Chen, N. Chen, Y. Hou, Z. C. Wang, S. H. Lv, T. Fujita, J. H. Jiang, A. Hirata, M. W. Chen, *ACS Catal.* **2013**, *3*, 1220 – 1230.
[19] K. M. Yeo, S. Choi, R. M. Anisur, J. Kim, I. S. Lee, *Angew. Chem. Int. Ed.* **2011**, *50*, 745 – 748; *Angew. Chem.* **2011**, *123*, 771 – 774.
[20] C. Koenigsmann, E. Sutter, T. A. Chiesa, R. R. Adzic, S. S. Wong, *Nano Lett.* **2012**, *12*, 2013 – 2020.
[21] X. Chen, G. Wu, J. Chen, X. Chen, Z. Xie, X. Wang, *J. Am. Chem. Soc.* **2011**, *133*, 3693 – 3695.
[22] Q. Wang, Y. Liao, H. Zhang, J. Li, W. Zhao, S. Chen, *J. Power Sources* **2015**, *292*, 72 – 77.
[23] A.-K. Herrmann, P. Formanek, L. Borchardt, M. Klose, L. Giebeler, J. Eckert, S. Kaskel, N. Gaponik, A. Eychmüller, *Chem. Mater.* **2014**, *26*, 1074 – 1083.
[24] J. Cui, H. Zhang, Y. Yu, Y. Liu, Y. Tian, B. Zhang, *J. Mater. Chem.* **2012**, *22*, 349 – 354.
[25] A. Rochefort, M. Abon, P. Delichère, J. C. Bertolini, *Surf. Sci.* **1993**, *294*, 43 – 52.
[26] Y. Ren, S. Zhang, R. Lin, X. Wei, *Int. J. Hydrogen Energy* **2015**, *40*, 2621 – 2630.
[27] C. Hu, K. Lin, X. Wang, S. Liu, J. Yi, Y. Tian, B. Wu, G. Chen, H. Yang, Y. Dai, H. Li, N. Zheng, *J. Am. Chem. Soc.* **2014**, *136*, 12856 – 12859.
[28] Y. Xia, Y. Xiong, B. Lim, S. E. Skrabalak, *Angew. Chem. Int. Ed.* **2009**, *48*, 60 – 103; *Angew. Chem.* **2009**, *121*, 62 – 108.
[29] T. Wu, H. M. Zhou, B. Y. Xia, P. Xiao, Y. Yan, M. S. Xie, X. Wang, *ChemCatChem* **2014**, *6*, 1538 – 1542.
[30] Y. Wang, J. He, C. Liu, W. H. Chong, H. Chen, *Angew. Chem. Int. Ed.* **2015**, *54*, 2022 – 2051; *Angew. Chem.* **2015**, *127*, 2046 – 2079.
[31] M.-W. Hsieh, T.-J. Whang, *Appl. Surf. Sci.* **2013**, *270*, 252 – 259.
[32] R. Mancharan, J. B. Goodenough, *J. Mater. Chem.* **1992**, *2*, 875 – 887.
[33] A. M. Hofstead-Duffy, D.-J. Chen, S.-G. Sun, Y. J. Tong, *J. Mater. Chem.* **2012**, *22*, 5205.

Received: August 28, 2015
Published online on October 16, 2015